J Mater Sci (2020) 55:11439–11450

Electronic materials

Ohmic contacts of monolayer Tl_2O field-effect transistors

Yuanyuan Pan[1], Jingrou Dai[1], Zihui Liu[1], Mingbo Wu[1,*], Han Hu[1,*], and Jing Lu[2,3,4,*]

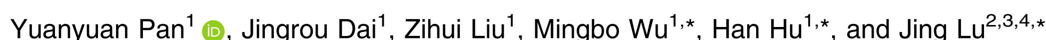

[1] State Key Laboratory of Heavy Oil Processing, Institute of New Energy, College of Chemical Engineering, China University of Petroleum (East China), Qingdao 266580, People's Republic of China
[2] State Key Laboratory for Mesoscopic Physics and Department of Physics, Peking University, Beijing 100871, People's Republic of China
[3] Collaborative Innovation Center of Quantum Matter, Beijing 100871, People's Republic of China
[4] Beijing Key Laboratory for Magnetoeletric Materials and Devices (BKL-MEMD), Beijing 100871, People's Republic of China

Received: 11 April 2020
Accepted: 22 May 2020
Published online:
2 June 2020

© Springer Science+Business Media, LLC, part of Springer Nature 2020

ABSTRACT

Monolayer (ML) Tl_2O, as a newly discovered metal-shrouded two-dimensional semiconductor with an appropriate bandgap and high carrier mobility, is a promising candidate as the channel materials for the next-generation field-effect transistors (FETs). Using ab initio electronic structure calculation and quantum transport simulation, the contact properties of ML Tl_2O–metal interfaces based on FET are comprehensively investigated with Au, Sc, Tl, Ni, graphene, Ti_2C, Ti_2CF_2, and $Ti_2C(OH)_2$ electrodes. ML Tl_2O undergoes metallization with Au, Sc, Tl, Ni, and Ti_2C, while it forms van der Waals-type contact with graphene, Ti_2CF_2, and $Ti_2C(OH)_2$. An *n*-type lateral Schottky contact is formed with Ni, Au, Sc, and Ti_2C electrodes with the electron Schottky barrier height (SBH) of 0.25, 0.27, 0.27, and 0.36 eV, respectively, while a *p*-type lateral Schottky contact is formed with graphene electrode with the hole SBH of 0.10 eV. Surprisingly, a desired *n*-type Ohmic contact arises with Tl and $Ti_2C(OH)_2$ electrodes and a desired *p*-type Ohmic contact arises with Ti_2CF_2 electrode. The study not only provides a deep understanding of the interfacial properties of the ML Tl_2O FETs but also reveals a versatile approach to realize both *n*- and *p*-type Ohmic contact for the ML Tl_2O FETs.

Introduction

Over the last decades, two-dimensional (2D) semiconductors have been drawing extensive attention for their intriguing physical properties and promising applications in nanoelectronic [1–3]. Due to improved carrier transport associated with the absence of dangling bond at the interface and the reduced scattering at smooth surface and remarkable gate electrostatics associated with atomically thin thickness, 2D semiconductors exhibit great potentials to be the channel

Address correspondence to E-mail: wumb@upc.edu.cn; hhu@upc.edu.cn; jinglu@pku.edu.cn

https://doi.org/10.1007/s10853-020-04866-2

materials beyond traditional semiconductors for the next-generation nanoelectronic devices [4–6]. A successful 2D semiconductor successor of traditional semiconductor not only requires an advisable bandgap greater than 0.4 eV [6] but also needs to meet two other criteria: ambient stability and high carrier mobility. 2D semiconductors, such as 2D MoS_2 and WSe_2, black phosphorene, and 2D InSe, are intensively researched for the electronics with the proper band gaps [7, 8]. Unfortunately, these 2D semiconductors cannot meet the other two criteria mentioned above. For example, 2D MoS_2 has relatively low carrier mobility that causes the low on-currents in experiments, which is less than 250 $\mu A\ \mu m^{-1}$ [9–11]. Although black phosphorene and 2D InSe possess high carrier mobility, their insufficient ambient stability results in the rapid degradation of device performance when exposed to the air [12–15]. Consequently, looking for a proper 2D semiconductor that meets all these criteria is critical.

Monolayer (ML) Tl_2O, the first metal-shrouded 2D semiconductor, has been recently predicted with a direct bandgap about 1.0 eV [16]. The calculated carrier mobility of ML Tl_2O is comparable to that of ML phosphorene and 2D InSe, which is up to $4.3 \times 10^3\ cm^2\ V^{-1}\ s^{-1}$. What is more, it is dynamically and thermally stable and is easy to be mechanically exfoliated from the bulk Tl_2O with a low exfoliation energy (0.43 $J\ m^{-2}$) [16, 17]. These characteristics indicate that ML Tl_2O is a promising candidate for the future high-performance and low-power nanoelectronic devices applications. In an actual transistor of 2D semiconductor, forming low-resistance contacts at the interfaces is just as important as the semiconducting characters itself [18–20]. Contacting with metal electrodes is inevitable in 2D semiconductors, and Schottky barrier and Fermi level pinning (FLP) effects always appear at the 2D semiconductors–metal interfaces in their transistors [21–23]. The interfacial properties of ML Tl_2O transistors are still exclusive, and forming Ohmic contacts of ML Tl_2O–metal interface is expected. 2D metals, such as graphene and MXene, are new and preferable choice for the metal electrodes, which can form low-resistance van der Waals (vdW)-stacked junctions with 2D semiconductors [24–28]. Particularly, the work function (WF) of MXene can be tuned by the functional group at the surfaces, indicating that the carrier polarity of 2D semiconductor field-effect transistor (FET) can be tuned by choosing the surficial functional group (Table 1).

In this article, based on the FET configuration, the interfacial properties between ML Tl_2O and eight metals (traditional bulk metals: Au, Sc, Tl, and Ni; 2D metals: graphene, Ti_2C, Ti_2CF_2, and $Ti_2C(OH)_2$) are systematically investigated by utilizing ab initio electronic structure calculations and quantum transport simulations. ML Tl_2O encounters a metallization contacting with Au, Sc, Tl, Ni, and Ti_2C electrodes, while it forms vdW-type contacts with graphene, Ti_2CF_2, and $Ti_2C(OH)_2$ electrodes with the band structure of ML Tl_2O kept. In the ML Tl_2O FETs, an *n*-type lateral Schottky contact is formed when Sc, Ni, Ti_2C, and Au are electrodes with the electron Schottky barrier height (SBH) of 0.27, 0.25, 0.35, and 0.27 eV, respectively, while a *p*-type lateral Schottky contact is formed when graphene is the electrode with the hole SBH of 0.10 eV. The desired *n*-type Ohmic contact is formed with $Ti_2C(OH)_2$ and Tl electrodes, and the desired *p*-type Ohmic contact is formed with Ti_2CF_2 electrode. Because of the metal-induced gap states (MIGS) and the interaction between the channel ML Tl_2O and the electrodes, strong FLP is discovered in the ML Tl_2O FETs with the pinning factor of 0.15.

Methodology

Interface and device models

Au, Ni, Sc, Tl, graphene, $Ti_2C(OH)_2$, Ti_2CF_2, and Ti_2C are taken into consideration as electrodes, which cover a wide range of WF. For bulk metal Au, Ni, Sc, and Tl, five layers of metal atoms are constructed to model the metal surface, while for two-dimensional metal graphene and Ti_2C without and with F/OH termination, ML structure is constructed. ML Tl_2O is absorbed on one side of the metal surfaces as shown in Fig. 1c. The lattice constant of ML Tl_2O is fixed with the optimized lattice constant $a = b = 3.59$ Å, and the lattice constants of metal surface are changed to adapt it correspondingly. The 1×1 unit cell of ML Tl_2O matches 1×1 unit cell of Sc and Tl surface, and the 2×2 unit cells of ML Tl_2O match 3×3 unit cell of Au (111), Ni (111), and graphene surface, and the $\sqrt{5} \times \sqrt{5}$ unit cells of ML Tl_2O match the 2×2 unit cells of Ti_2C, Ti_2CF_2, and $Ti_2C(OH)_2$ surfaces. The mismatches of lattice constant with $Ti_2C(OH)_2$,

Table 1 Calculated interfacial properties of the ML Tl_2O–metal contacts

	Graphene	Ti_2CF_2	$Ti_2C(OH)_2$	Ti_2C	Tl	Au	Sc	Ni
$\bar{\varepsilon}$ (%)	1.79	1.10	0.56	1.51	2.62	3.89	3.96	2.59
d_z (Å)	3.45	2.97	3.32	2.54	3.18	2.76	2.61	2.29
E_b (eV)	0.30	0.24	0.43	1.29	0.50	0.63	0.97	1.36
$W_{T\text{-}M}$ (eV)	4.22	4.81	1.10	3.98	3.48	4.70	3.52	4.60
W_M (eV)	3.91	4.92	1.66	4.43	3.35	5.07	3.68	5.18
$\Phi_L^{e,\text{trans}}$ (eV)	0.92	0.98	0.00	0.36	0.00	0.27	0.27	0.25
$\Phi_L^{h,\text{trans}}$ (eV)	0.10	0.00	1.02	0.65	0.95	0.77	0.71	0.90
E_g^{trans} (eV)	1.02	0.98	1.02	1.01	0.95	1.04	0.98	1.15
L (nm)	5.0	5.4	5.4	5.6	5.6	5.0	5.6	5.2

$\bar{\varepsilon}$ is the absolute average lattice constant mismatch of the ML Tl_2O–metal interface. The equilibrium distance d_z is the average distance of the ML Tl_2O–metal interfaces in the vertical direction. The binding energy E_b is the energy of per ML Tl_2O being removed from metal surface. W_M and $W_{T\text{-}M}$ are the calculated work function for the clean metals surface and the ML Tl_2O–metal system, respectively. $\Phi_L^{e,\text{trans}}$ ($\Phi_L^{h,\text{trans}}$) is the electron (hole) SBH in the lateral direction obtained by quantum transport simulation. E_g^{trans} is the transport gap, defined as $E_g^{\text{trans}} = \Phi_L^{e,\text{trans}} + \Phi_L^{h,\text{trans}}$. L is the channel length of the ML Tl_2O FETs. The calculated work function of the pristine ML Tl_2O is W = 4.59 eV

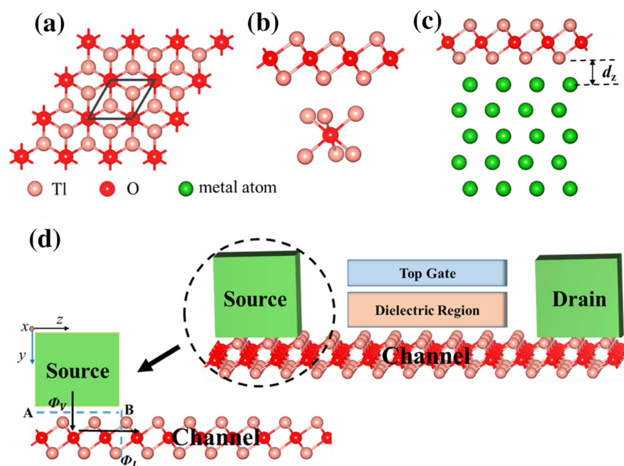

Figure 1 **a** Top and **b** side views of the free-standing ML Tl_2O. The rhombus indicates the unit cell of ML Tl_2O. **c** Atomic configuration of ML Tl_2O–metal interfaces. **d** Schematic diagram of a ML Tl_2O FET at the upper-right portion. The enlarged picture of the electrode region at the lower-left portion. Black rows represent the pathways that the carrier transfers from the electrode to the channel ML Tl_2O. Blue dashed lines indicate two interfaces at ML Tl_2O FET, *i.e.*, vertical interface A and lateral interface B. Φ_V and Φ_L represent the corresponding vertical and lateral SBH, respectively.

Ti_2CF_2, Ti_2C, graphene, Ni, Tl, Au, and Sc surfaces are 0.56%, 1.10%, 1.51%, 1.79%, 2.59%, 2.62%, 3.89%, and 3.96%, respectively. ML Tl_2O mainly couples with the top three layers of metal atoms for Ni, Tl, Au, and Sc [29], so the bottom two layers of the metal atom freeze in the geometry optimizations.

We build a two-probe ML Tl_2O FET to study its interfacial properties as shown in Fig. 1d. Pristine ML Tl_2O is used in the channel region with the channel length of 5–6 nm along the transport direction, and the optimized ML Tl_2O–metal interfaces are used in the left and the right electrode region with semi-infinite length.

Computational methods

The geometry optimizations and the electronic properties of the ML Tl_2O–metal interfaces are calculated based on density functional theory (DFT) performed in the Vienna ab initio simulation package (VASP) code [30–32]. Ion–electron interactions are described by utilizing projected augmented wave (PAW) approximation [33]. The plane-wave basis is applied with cut-off energy of 500 eV. In the interfacial systems, vdW correction is processed by zero damping DFT-D3 method of Grimme [34]. The convergence threshold for the residual force is not more than 0.01 eV/Å and the energy difference converges to 1×10^{-6} eV for per atom during geometry optimization. The Monkhorst–Pack k-point grid is sampled in the Brillouin zone [35] with a separation of 0.02 $Å^{-1}$. To satisfy decoupling between the adjacent slabs, the vacuum buffer layer is set at least 15 Å.

DFT combining with nonequilibrium Green's function (NEGF) method is applied for the ML Tl_2O FET calculations, which are carried out in Atomistix

ToolKit (ATK) 2019 package [36–38]. The transmission coefficient $T(k_y, E)$ is defined by the following equation:

$$T(k_y, E) = Tr[\Gamma_L(k_y, E)G(k_y, E)\Gamma_R(k_y, E)G^+(k_y, E)]$$

where $G(k_y, E)$ ($G^+(k_y, E)$) represent a retarded (advanced) Green function in the central region and k_y is the y portion of the reduced wave vector. (The coordinate axis is labeled in Fig. 1d.) The self-energy correction term $\Gamma_{L/R} = i(\sum_{L/R}^r - \sum_{L/R}^a)$ expresses the level broadening that is produced by the interaction between the center region and the electrode, and the electrode self-energy can be regarded as an effective Hamiltonian to describe the interplay between the lead and the device [39]. In the simulations, temperature is set to 300 K. The linear combination of the atomic orbits (LCAO) basis set with the double-ξ polarization (DZP) form is taken into account. The Monkhorst–Pack [35] k-point meshes are sampled in the device with a separation of 0.08 Å^{-1} in x orientation and 0.007 Å^{-1} in z orientation. The Periodic, Neumann, and Dirichlet boundary condition are implemented in the x, y, z orientation of the ML Tl_2O FETs, respectively.

In the paper, the generalized gradient approximation (GGA) of Perdew–Burke–Ernzerhof (PBE) method is adopted to describe the exchange and correlation interactions [40, 41]. When contacting with metals, 2D semiconductors are significantly doped with the carrier. Electron–electron interactions are screened in the doped 2D semiconductor, and thus, DFT–GGA comes to be a good approximation for the estimation of the bandgap and Schottky barriers [42, 43]. For instance, the bandgap of the doped ML $MoSe_2$ obtained at the DFT–GGA level of 1.53 eV is in good agreement with that derived from the GW calculation of 1.59 eV [43]. What is more, the SBH in ML/bilayer/trilayer phosphorene FET is well reproduced, i.e., the calculated electron SBHs of 0.34/0.19/0.20 eV at the DFT–GGA level are well kept with those of 0.39/0.23/0.21 eV from the experimental measurements [44–47].

Results and discussion

Configuration and bonding degree of ML Tl_2O–metal interfaces

After optimization, the atomic configurations of the ML Tl_2O–metal interfaces are presented in Fig. 2 and figure S1. The geometrical structure of ML Tl_2O is well maintained on all the metal surfaces. On Ni (111) and Au (111) surface, both the Tl and O atoms are almost located in the center of the triangle formed by the three layers of metal atoms; on the Tl and Sc (0001) surface, the Tl atoms exactly sit above the metal atoms, and the O atoms sit above the center of the hexagon of metal atoms; on Ti_2C surface, the O atoms sit above the topmost Ti atoms and C atoms, and the Tl atoms sit above the center of triangle shown in figure S1(i); on graphene, Ti_2CF_2, and $Ti_2C(OH)_2$ surfaces, the O and Tl atoms are randomly scattered on these metal surfaces.

To illustrate the binding level of these interfaces, we have calculated the binding energy and the interlayer distance. The binding energy E_b between ML Tl_2O and metals is defined as follows:

$$E_b = (E_T + E_M - E_{T-M})/N$$

where E_T, E_M, and $E_{S\text{-}M}$ stand for the optimized energy for the free-standing ML Tl_2O, the clean crystalline metal, and the corresponding combined system per supercell, respectively, and the N denotes the number of Tl atom in the sublayer near metals per supercell. The equilibrium separation of the interlayer d_z is the average distance in the vertical direction to the interfaces between the nearest metal atom layer to ML Tl_2O and the neighboring Tl atom layer as indicated in Fig. 1c. According to the binding energy and the equilibrium interlayer distance, the ML Tl_2O–metal interfaces are divided into three categories. Weak bonding is formed for the ML Tl_2O–Ti_2CF_2, $Ti_2C(OH)_2$, and graphene interfaces with $2.97 < d_z < 3.45$ Å and $0.24 < E_b < 0.43$ eV; medium bonding is formed for the ML Tl_2O–Tl interface with $d_Z = 3.18$ Å and $E_b = 0.50$ eV; strong bonding is formed for the ML Tl_2O–Au, Sc, Ti_2C, and Ni interfaces with $2.29 < d_z < 2.76$ Å and $0.63 < E_b < 1.36$ eV. In the case of the weak bonding, the small binding energy suggests that vdW-type stacking is formed between ML Tl_2O and graphene, Ti_2CF_2, and $Ti_2C(OH)_2$. In the most cases, the binding degree of ML Tl_2O with metals is stronger than that of ML transition-metal dichalcogenides (TMDs) with metals, such as the binding energy of ML Tl_2O vs. ML MoS_2 (Ni: 1.36 > 0.83 eV; Au: 0.63 > 0.307 eV) [48, 49]. This may be because the metal-shrouded ML Tl_2O with Tl atoms is more active than the nonmetal-shrouded ML TMDs.

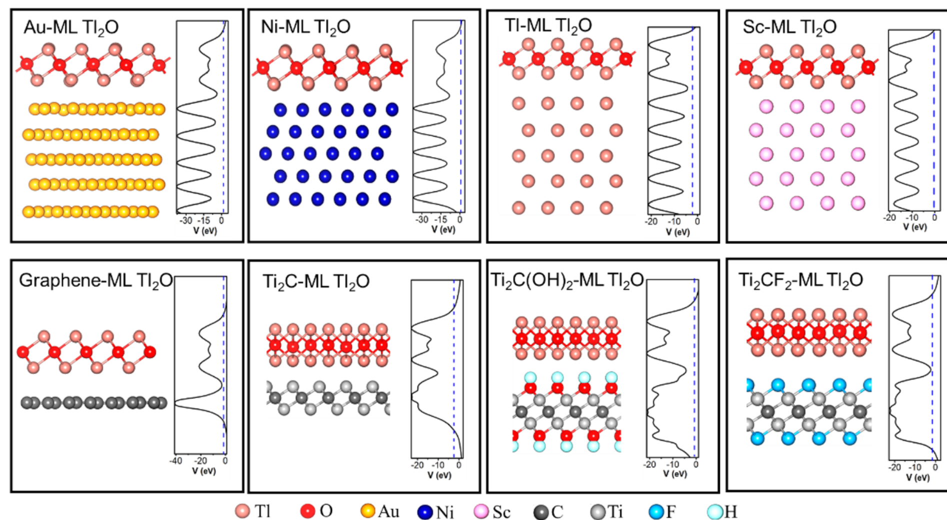

Figure 2 Side view of the optimized atomic structures and average electrostatic potential distributions in the planes normal to the interfaces of ML Tl_2O on Au, Ni, Tl, Sc, graphene, Ti_2C, $Ti_2C(OH)_2$, and Ti_2CF_2 surfaces. The Fermi level is represented by blue dashed lines.

Electronic structure of ML Tl_2O–metal interfaces

The band structures of the pristine ML Tl_2O and the interfacial systems are shown in Fig. 3. The free-standing ML Tl_2O is a semiconductor with a direct bandgap of 1.0 eV located at M point by the plane-wave basis set with the PBE level, which agrees with the previous theoretical results [14]. The bandgap of ML Tl_2O is also calculated by the DZP basis set in the ATK package with the same value of 1.0 eV as shown

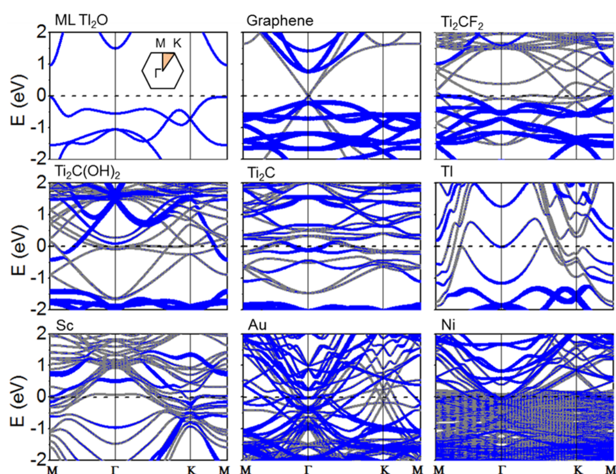

Figure 3 Band structures of the pristine ML Tl_2O and the ML Tl_2O–graphene, Ti_2CF_2, $Ti_2C(OH)_2$, Ti_2C, Tl, Sc, Au, and Ni interfaces. Gray lines represent the band structure of the interfacial systems, and blue lines represent the band structure projected to the ML Tl_2O in the interfacial systems. The line width is proportional to the weight. The Fermi level is set at zero energy and denoted by the black dashed lines. The inset graph shows the Brillouin zone.

in figure S2. The effective mass m^* ($\frac{1}{m^*} = \frac{1}{\hbar^2}\frac{d^2E}{dk^2}$) is calculated by the band structure of ML Tl_2O. The band near the conduction band minimum (CBM) is relatively steep, bringing about a really small electron effective mass of $0.18m_e$ and $0.62m_e$ (m_e is the mass of an electron) along M → Γ and M → K direction, respectively; the band near the valence band maximum (VBM) along M → Γ direction is also quite steep, resulting in a small hole effective mass of $0.37m_e$. On the contrary, the band near the VBM along M → K direction is flat, resulting in a large hole effective mass of $5.90m_e$. The calculated effective masses are well consistent with the previous results [50]. The small effective masses promise a large carrier mobility comparable to that of black phosphorene [51, 52].

The band structures of the ML Tl_2O in the interfacial systems, which reflect the difference of the bonding level, are shown in Fig. 3. In the weak bonding, although band folding exists owing to the supercell calculation, the intrinsic band structure of ML Tl_2O is preserved with the formation of the vdW-type interactions. The bandgap is maintained with the value of 0.92, 0.98, and 1.00 eV after contacting with graphene, Ti_2CF_2, and $Ti_2C(OH)_2$, respectively. Electron transfer occurs at these interfaces, which leads to the energy level shift of the ML Tl_2O. As for the medium and the strong bonding with Tl, Au, Sc, Ti_2C, and Ni electrode, the band structures of the ML Tl_2O are destroyed with the bandgap disappearing, resulting in the metallization of the ML Tl_2O. It is found that although the ML Tl_2O-Tl system has a smaller E_b and a larger d_z than the strong bonding,

the energy band structure of ML Tl_2O is also heavily hybridized resulting from the consistency of the orbital of Tl atoms in the metal substrates and the ML Tl_2O.

In order to get a deeper insight into the electronic properties of the ML Tl_2O contacted with metals, we further analyze the partial density of states (PDOS) of the ML Tl_2O in the interfacial systems, as shown in Fig. 4. In agreement with the band structure, the bandgap of the ML Tl_2O is kept in the case of the weak bonding with the value of 0.90, 0.89, and 0.85 eV in contacting with graphene, $Ti_2C(OH)_2$, and Ti_2CF_2 electrodes, respectively. By contrast, a large amount of DOS are extended into the bandgap of the ML Tl_2O in the case of the medium and the strong bonding, and thus, electron state appears at the Fermi level, which is a typical character of metallization. The DOS near the CBM is mainly composed of *s* and *p* orbitals, while that near the CBM is mainly composed of $p_x + p_y$ orbitals in the free-standing ML Tl_2O. The orbital component of the ML Tl_2O in the case of the weak bonding interfacial systems is similar to that of the free-standing ML Tl_2O. In the medium and strong bonding case, the *s* and *p* orbitals of the metalized ML Tl_2O nearly make the same contributions at the Fermi level. To further visualize the physical picture of the interaction at the interface, the real-space total electron distribution of a slice that crosses both ML Tl_2O and metal atoms is plotted in figure S3. There is apparently more electron accumulation at the interfaces for the medium and strong binding (ML Tl_2O–Ti_2C, Tl, Au, Sc, and Ni interfaces) than that for the weak binding interfaces (ML Tl_2O–$Ti_2C(OH)_2$, Ti_2CF_2 and graphene interfaces).

Schottky barriers in ML Tl_2O FETs

When electron transfers from the metal electrode to the channel ML Tl_2O, it will encounter two kinds of interfaces: One is between metal electrode and the underneath contacted ML Tl_2O in the vertical direction, which is called vertical interface (labeled as interface A in Fig. 1d); the other is between the ML Tl_2O–metal systems and the channel ML Tl_2O in the lateral direction, which is called the lateral interface (labeled as interface B in Fig. 1d). There may be Schottky barrier and tunneling barrier at the two interfaces. For the weak bonding (the vdW-type interactions) with the band structures of ML Tl_2O preserved, Schottky barrier and tunneling barrier may appear at the vertical interfaces A. However, for the medium and strong bonding, Schottky barrier and tunneling barrier will disappear at the vertical interfaces A owing to the metallization of the underneath contacted ML Tl_2O. The metalized ML Tl_2O–metal systems are treated as a new metal system, and therefore, lateral Schottky barrier may exist at the interfaces B. Tunneling barrier is determined

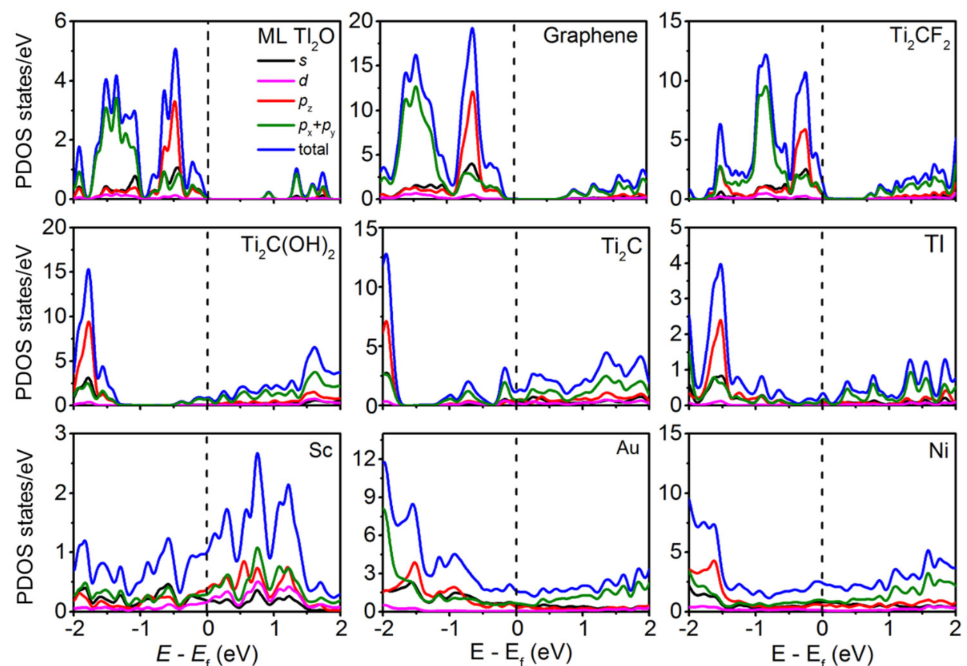

Figure 4 Partial density of states (PDOS) (DOS on the specified orbitals) of the pristine ML Tl_2O and ML Tl_2O on the graphene, Ti_2CF_2, $Ti_2C(OH)_2$, Ti_2C, Tl, Sc, Au, and Ni surfaces. The Fermi level is set at zero. The PDOS of the pristine ML Tl_2O is calculated in the primitive unit cell.

by the electrostatic potential barrier going through the Fermi level at the ML Tl_2O–metal interfaces. Figure 2 shows the average electrostatic potential profiles normal to the interface between ML Tl_2O and metals. Apparently, the electrostatic potential is below the Fermi level at the interfaces, so the tunneling barrier is zero in all the checked systems.

The vertical electron/hole Schottky barrier Φ_V^e / Φ_V^h is defined as the energy difference between the Fermi level of the interfacial systems and the VBM/CBM of the ML Tl_2O in electrode. From the band structure analysis, a *p*-type and an *n*-type vertical Ohmic contact are formed with Ti_2CF_2 and $Ti_2C(OH)_2$, respectively, because of the Fermi level of the interfacial systems under the VBM or above the CBM of the ML Tl_2O. When contacting with graphene, a *p*-type vertical Schottky contact is established, and the hole vertical SBH is 0.10 eV. Due to the metallization of ML Tl_2O under the metal electrodes, vertical Ohmic contact is formed at the ML Tl_2O-Tl, Au, Sc, Ti_2C, and Ni interfaces.

The commonly used method to examine the lateral SBH is work function approximation (WFA), in which the lateral electron/hole SBH $\Phi_L^{e,WFA}/\Phi_L^{h,WFA}$ is determined by the energy difference between the CBM/VBM of the channel materials and the Fermi level of the interfacial systems. We plot the band alignment of the free-standing ML Tl_2O and line-up of the WF of the interfacial systems in Fig. 5. An *n*-type lateral Ohmic contact is formed with $Ti_2C(OH)_2$, Tl, and Sc electrodes, while a *p*-type lateral Ohmic contact is established with Ti_2CF_2 and Au electrodes in ML Tl_2O FETs. What is more, an *n*-type Schottky contact is established with Ti_2C electrode with the lateral electron SBH $\Phi_L^{e,WFA}$ of 0.37 eV, and a *p*-type Schottky contact is established with graphene and Ni electrodes with the lateral hole SBHs $\Phi_L^{h,WFA}$ of 0.39 and 0.01 eV, respectively.

The electrode and the channel ML Tl_2O are treated as the independent parts in the WFA, and thus, the coupling between the two parts is ignored. The more direct and reliable method to calculate the lateral SBH in 2D semiconductor FETs is ab initio quantum transport simulation based on a real two-probe FET model with including the coupling. For example, the calculated SBHs of ML, bilayer, and trilayer black phosphorene with Ni electrode by quantum transport simulations are 0.34, 0.19, 0.20 eV, respectively, consistent well with that of 0.39, 0.23, and 0.21 eV in the experimental measurements [44–46]. The SBHs of ML MoS_2 with Au and Pd electrodes by quantum transport simulations are in better agreement with those observed in experiments than that by the WFA [22, 49, 53, 54].

The transport properties of the two-probe ML Tl_2O FETs are calculated by using the quantum transport simulation. Figure 6 is the local device density of states (LDDOS) of ML Tl_2O FETs under zero-bias and zero-gate voltage with graphene, Ti_2CF_2, $Ti_2C(OH)_2$, Ti_2C, Ni, Au, Tl, and Sc electrodes, where the density of states is projected into the ML Tl_2O. In the electrode regions, the hybridization degree of the electronic band for the ML Tl_2O is well consistent with that in the band structure. The bandgap of ML Tl_2O is well preserved when contacting with the graphene, Ti_2CF_2, and $Ti_2C(OH)_2$, while the band structure of ML Tl_2O hybridizes with that of the metal electrode when contacting with Ti_2C, Au, Ni, Sc, and Tl. According to the energy-level distribution in the electrode region, a *p*-type vertical Schottky contact is established with the SBH of 0.1 eV for graphene, while an *n*-type and a *p*-type Ohmic contact are established with $Ti_2C(OH)_2$ and Ti_2CF_2 electrode, respectively. Because of electron transfers from Ti_2CF_2 electrodes to the channel ML Tl_2O, the CBM of the ML Tl_2O is obviously bent downward at the interface. The band hybridization of ML Tl_2O makes carrier directly go thorough from the metal to the underneath ML Tl_2O without vertical Schottky barrier with Ti_2C, Au, Ni, Sc, and Tl electrodes.

According to the LDDOS of ML Tl_2O FET at the lateral interface, it is found that ML Tl_2O forms *n*-type lateral Schottky contact with Ti_2C, Sc, Au, and Ni electrodes with the lateral electron SBHs $\Phi_L^{e,trans}$ of 0.36, 0.27, 0.27, and 0.25 eV, respectively. For the Tl electrode, the Fermi level is above the CBM of ML Tl_2O at the interfaces indicating that an *n*-type Ohmic contact is established in ML Tl_2O FETs. Transmission gap is defined as the sum of the lateral holes and electrons SBH: $E_g^{trans}=\Phi_L^{e,trans}+\Phi_L^{h,trans}$. The transport gap of ML Tl_2O FETs extracted from the LDDOS is 1.15, 1.02, 1.04, 1.02, 1.01, 0.98, 0.98, and 0.95 eV with Ni, graphene, Au, $Ti_2C(OH)_2$, Ti_2C, Ti_2CF_2, Sc, and Tl electrodes, respectively. The transport band gaps are similar to the bandgap of the free-standing ML Tl_2O.

The transmission spectrum of the ML Tl_2O FETs under zero-bias and gate voltage is plotted in Fig. 6 (right side of each figure). When Ti_2C, Au, Ni, and Sc

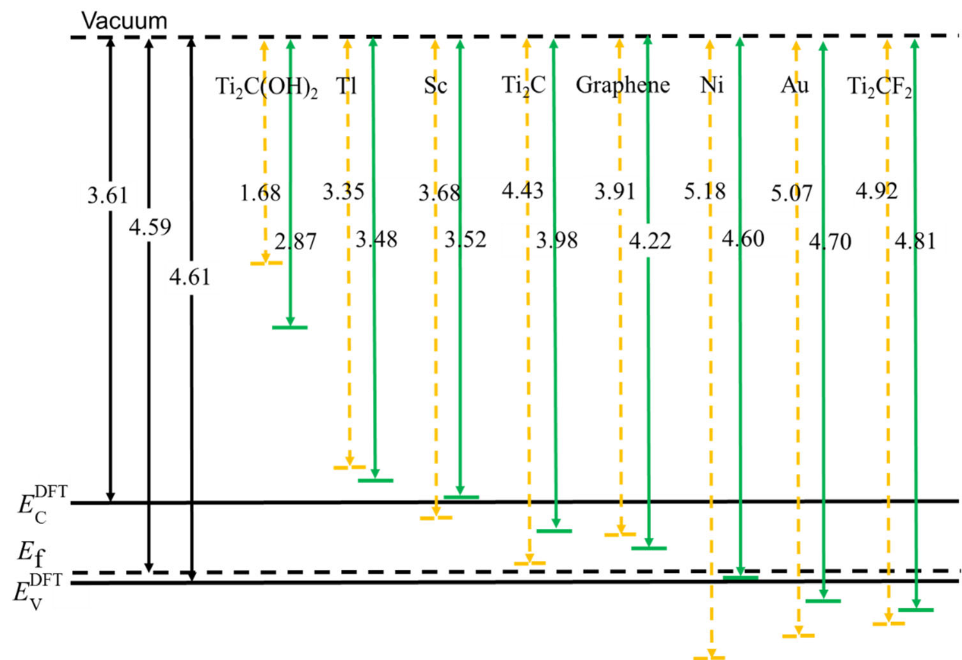

Figure 5 Band alignment of the free-standing ML Tl_2O and line-up of the work functions of the interfacial systems in terms of separate electronic energy band calculations. E_f denotes the Fermi level of the ML Tl_2O. E_C^{DFT} and E_V^{DFT} are the conduction and valence band edges of the ML Tl_2O calculated at DFT level, respectively. The orange dashed and the green solid lines present the work functions of the pristine metals and the corresponding ML Tl_2O–metals systems, respectively. The unit of the data in the figure is eV.

are used as electrodes, *n*-type FETs are established with the electron SBHs of 0.33, 0.29, 0.28, and 0.24 eV, respectively. When graphene is used as electrode, a *p*-type Schottky FET is established with the hole SBH of 0.14 eV. Obviously, Tl and $Ti_2C(OH)_2$ electrodes form the desired *n*-type Ohmic contacts, and Ti_2CF_2 electrode forms an expected *p*-type Ohmic contact in ML Tl_2O FETs. The height and polarity of the lateral Schottky barrier calculated by the transmission spectrum are generally consistent with those obtained from the LDDOS.

The desired Ohmic contact is realized with $Ti_2C(OH)_2$ and Ti_2CF_2 electrodes in the ML Tl_2O FETs, and the carrier polarity is changed from *n*-type with OH functional group to *p*-type with F functional group. The modulation of the contact type with the terminal Ti_2C electrodes is beneficial from the significant difference of WF for Ti_2C with different functional groups. For example, the WFs of $Ti_2C(OH)_2$ and Ti_2CF_2 are 1.10 and 4.81 eV, respectively. The phenomenon is also reported in the ML MoS_2 counterpart [55]. What is more, weak vdW junction is always formed between the ML Tl_2O and terminated Ti_2C with functional group, and the band structures of the ML Tl_2O are preserved, which favors the performance of 2D semiconductor FETs. Thus, MXene is an excellent electrode candidate for the ML Tl_2O FETs, and the contact can be tuned by changing the functional group at the surface of MXene.

Discussions

The polarity and height of the lateral Schottky barriers obtained from the quantum transport simulation and the WFA are compared in Fig. 7. The carrier polarity of the ML Tl_2O FETs is the same in the two methods for Sc, Tl, Ti_2C, graphene, $Ti_2C(OH)_2$, and Ti_2CF_2 electrodes, while it is completely reversed in the two approaches for Au and Ni electrodes. The *n*-type lateral Schottky contacts in the quantum transport simulations are changed into *p*-type Ohmic contact and quasi-Ohmic contact in the WFA for Au and Ni electrode, respectively. The SBH of the ML Tl_2O FET is similar for Ti_2C electrode by using the two approaches; Ohmic contacts are both formed when $Ti_2C(OH)_2$, Tl, and Ti_2C as electrodes in the two approaches; the SBH of ML Tl_2O FET is overestimated by the WFA than the quantum transport simulation for graphene electrode; a false Ohmic contact is examined with Sc electrode by using WFA. The discrepancy of the Schottky barrier of the two approaches is huge for the ML Tl_2O–metal contact, and the phenomena are common in the FET of 2D semiconductors [44, 48, 49]. The cause of the discrepancy is that the interaction between the electrode and the channel region is taken into consideration in the quantum transport simulations, but it is neglected in the WFA. The interaction is weak in the case of the weak binding ($Ti_2C(OH)_2$, Ti_2CF_2, and graphene

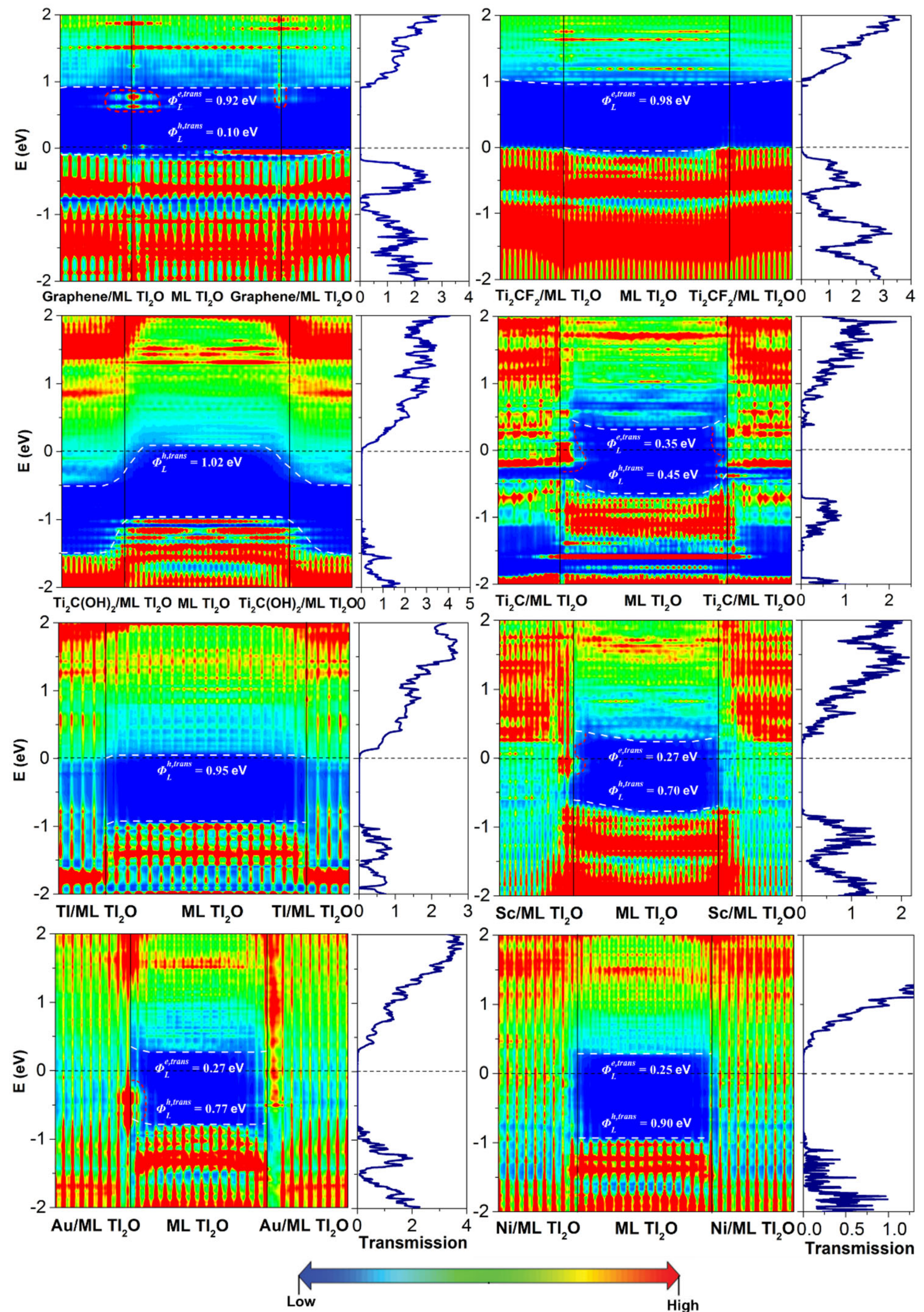

Figure 6 Zero-bias and zero-gate voltage LDDOS (left panel) and transmission spectra (right panel) of the ML Tl_2O FETs with graphene, Ti_2CF_2, $Ti_2C(OH)_2$, Ti_2C, Tl, Sc, Au, and Ni electrodes. The Fermi level is represented by the black dash line. The white dash lines represent the VBM and the CBM of the channel ML Tl_2O. The MIGS are represented by the red short dash lines.

electrodes), and the two methods give similar Schottky barrier. However, the interaction is strong in the strong binding case (ML Tl_2O-Ti_2C Tl, Sc, Au, and Ni electrodes), and the two approaches give the apparently different Schottky barrier type and height. The quantum transport simulation is more reliable to examine the lateral SBH by using a real two-probe model.

Strong FLP effect always occurs at 2D semiconductor–metal interfaces, such as for ML MoS_2 [22] and black phosphorene [44, 56], and the degree of FLP is decided by the pinning factor S, which is described by the following equation:

$$S = \mathrm{d}\Phi^{e}/\mathrm{d}W_{m} \tag{1}$$

where Φ^{e} denotes the SBH of the electron and W_{m} is the WF of the pristine metal. The Φ^{e} as a function of

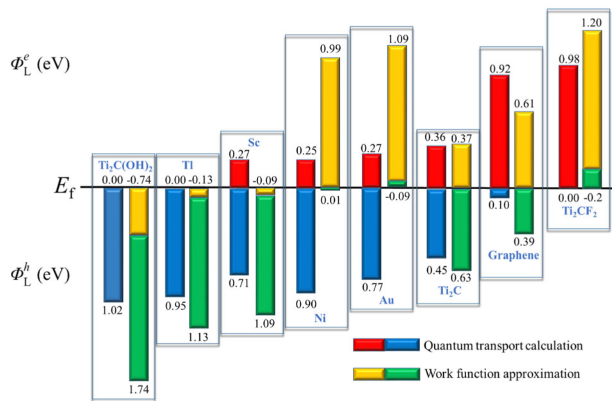

Figure 7 Comparison of the lateral SBHs obtained by the ab initio work function approximation and quantum transport calculation for the ML Tl_2O–$Ti_2C(OH)_2$, Tl, Sc, Ni, Au, Ti_2C, graphene, and Ti_2CF_2 interfaces. E_f is the Fermi level. Φ_L^e and Φ_L^h represent the lateral electron and hole SBH, respectively.

the W_m is plotted in Fig. 8. The value of pinning factor is 0.15 by using the quantum transport calculation, indicating a strong FLP appearing between the ML Tl_2O and metals. The strong FLP is from the MIGS, which apparently appears at the lateral interfaces with graphene, Ti_2C, Sc, and Au electrodes, as presented in Fig. 6. The other reason for the strong FLP is the interaction between the channel ML Tl_2O and the metal electrode considered in the quantum transport simulation. The pinning factor calculated by the WFA is 0.54 without including the coupling, which is apparently larger than that (0.15) calculated by the quantum transport simulation. The FLP effect

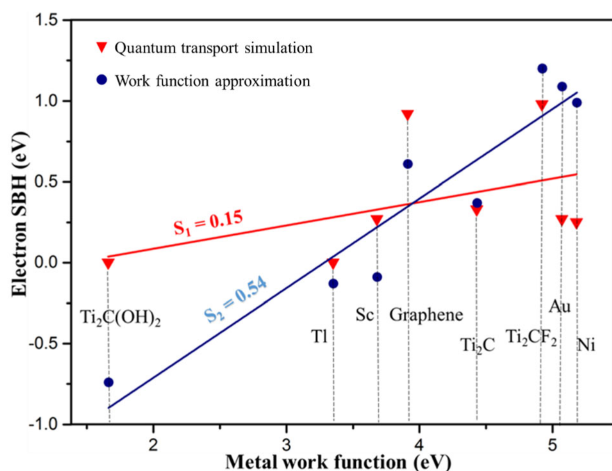

Figure 8 Relative electron SBH of the metal–ML Tl_2O junctions versus the work function values of metals. S is the pinning factor according to the Schottky–Mott rule.

of the ML Tl_2O FET is comparable with that of the ML MoS_2 FET with the pinning factor of 0.187 [53].

Conclusions

In conclusion, on the basis of ab initio electronic structure calculation and the quantum transport simulation, the interfacial properties of the ML Tl_2O FETs are comprehensively investigated with Au, Sc, Tl, Ni, graphene, Ti_2C, Ti_2CF_2, and $Ti_2C(OH)_2$ electrodes. The n-type Schottky FETs are discovered with Ni, Au, Sc, and Ti_2C electrodes with the lateral electron SBH of 0.25, 0.27, 0.27, and 0.36 eV, respectively, while the p-type Schottky FET is discovered with graphene electrode with the lateral hole SBH of 0.10 eV. Surprisingly, the desired n-type Ohmic contacts arise with Tl and $Ti_2C(OH)_2$ electrodes, and a desired p-type Ohmic contact arises with Ti_2CF_2 electrode in the ML Tl_2O FETs. Strong FLP is observed in the ML Tl_2O FETs with a small pinning factor of 0.15, which is mainly from the MIGS and the coupling between the electrode and the channel ML Tl_2O. Our result reveals a versatile approach to realize both n- and p-type Ohmic contact in the ML Tl_2O FETs.

Acknowledgements

This study was funded by the National Natural Science Foundation of China (Nos. 51572296, U1662113, 11904409), the Ministry of Science and Technology of China (No. 2016YFA0301300), the Fundamental Research Funds for the Central Universities (Nos. 17CX06029, 19CX05002A), China Postdoctoral Science Foundation (No. 2018M642721), and Shandong Postdoctoral Funded Project (201901012).

Compliance with ethical standards

Conflict of interest The authors declared that they have no conflict of interest.

Electronic supplementary material: The online version of this article (https://doi.org/10.1007/s10853-020-04866-2) contains supplementary material, which is available to authorized users.

References

[1] Geng D, Yang HY (2018) Recent advances in growth of novel 2D materials: beyond graphene and transition metal dichalcogenides. Adv Mater 30(45):1800865

[2] Zeng M, Xiao Y, Liu J, Yang K, Fu L (2018) Exploring two-dimensional materials toward the next-generation circuits: from monomer design to assembly control. Chem Rev 118(13):6236–6296

[3] Xu M, Liang T, Shi M, Chen H (2013) Graphene-like two-dimensional materials. Chem Rev 113(5):3766–3798

[4] Desai SB, Madhvapathy SR, Sachid AB, Llinas JP, Wang Q, Ahn GH, Pitner G, Kim MJ, Bokor J, Hu C, Wong HSP, Javey A (2016) MoS_2 transistors with 1-nanometer gate lengths. Science 354(6308):99–102

[5] Allain A, Kang J, Banerjee K, Kis A (2015) Electrical contacts to two-dimensional semiconductors. Nat Mater 14:1195–1205

[6] Schwierz F (2010) Graphene transistors. Nat Nanotechnol 5:487–496

[7] Fiori G, Bonaccorso F, Iannaccone G, Palacios T, Neumaier D, Seabaugh A, Banerjee SK, Colombo L (2014) Electronics based on two-dimensional materials. Nat Nanotechnol 9(10):768–779

[8] Chhowalla M, Jena D, Zhang H (2016) Two-dimensional semiconductors for transistors. Nat Rev Mater 1(11):1–15

[9] Xie L, Liao M, Wang S, Yu H, Du L, Tang J, Zhao J, Zhang J, Chen P, Lu X, Wang G, Xie G, Yang R, Shi D, Zhang G (2017) Graphene-contacted ultrashort channel monolayer MoS_2 transistors. Adv Mater 29(37):1702522

[10] Ni Z, Ye M, Ma J, Wang Y, Quhe R, Zheng J, Dai L, Yu D, Shi J, Yang J, Watanabe S, Lu J (2016) Performance upper limit of sub-10 nm monolayer MoS_2 transistors. Adv Electron Mater 2(9):1600191

[11] Xu K, Chen D, Yang F, Wang Z, Yin L, Wang F, Cheng R, Liu K, Xiong J, Liu Q, He J (2017) Sub-10 nm nanopattern architecture for 2D material field-effect transistors. Nano Lett 17(2):1065–1070

[12] Ho P-H, Chang Y-R, Chu Y-C, Li M-K, Tsai C-A, Wang W-H, Ho C-H, Chen C-W, Chiu P-W (2017) High-mobility InSe transistors: the role of surface oxides. ACS Nano 11(7):7362–7370

[13] Bandurin DA, Tyurnina AV, Yu GL, Mishchenko A, Zólyomi V, Morozov SV, Kumar RK, Gorbachev RV, Kudrynskyi ZR, Pezzini S, Kovalyuk ZD, Zeitler U, Novoselov KS, Patanè A, Eaves L, Grigorieva IV, Fal'ko VI, Geim AK, Cao Y (2017) High electron mobility, quantum Hall effect and anomalous optical response in atomically thin InSe. Nat Nanotechnol 12(3):223–227

[14] Li L, Yu Y, Ye GJ, Ge Q, Ou X, Wu H, Feng D, Chen XH, Zhang Y (2014) Black phosphorus field-effect transistors. Nat Nanotechnol 9:372–377

[15] Du Y, Liu H, Deng Y, Ye PD (2014) Device perspective for black phosphorus field-effect transistors: contact resistance, ambipolar behavior, and scaling. ACS Nano 8(10):10035–10042

[16] Ma Y, Kuc A, Heine T (2017) Single-layer Tl_2O: a metal-shrouded 2D semiconductor with high electronic mobility. J Am Chem Soc 139(34):11694–11697

[17] Wang H, Zhou Y, Zeng Z-Y, Cheng Y, Chen Q-F (2019) First-principles study of elastic, thermal and optical properties of a metal-shrouded two-dimensional semiconductor Tl_2O. Solid State Commun 293:40–47

[18] Kang J, Liu W, Sarkar D, Jena D, Banerjee K (2014) Computational study of metal contacts to monolayer transition-metal dichalcogenide semiconductors. Phys Rev X 4(3):031005

[19] Iannaccone G, Bonaccorso F, Colombo L, Fiori G (2018) Quantum engineering of transistors based on 2D materials heterostructures. Nat Nanotechnol 13(3):183–191

[20] Radisavljevic B, Radenovic A, Brivio J, Giacometti V, Kis A (2011) Single-layer MoS_2 transistors. Nat Nanotechnol 6:147–150

[21] Gong C, Colombo L, Wallace RM, Cho K (2014) The unusual mechanism of partial Fermi level pinning at metal–MoS_2 interfaces. Nano Lett 14(4):1714–1720

[22] Kim C, Moon I, Lee D, Choi MS, Ahmed F, Nam S, Cho Y, Shin HJ, Park S, Yoo WJ (2017) Fermi level pinning at electrical metal contacts of monolayer molybdenum dichalcogenides. ACS Nano 11(2):1588–1596

[23] Tung RT (2000) Chemical bonding and Fermi level pinning at metal-semiconductor interfaces. Phys Rev Lett 84(26):6078–6081

[24] Liu Y, Xiao H, Goddard WA (2016) Schottky-barrier-free contacts with two-dimensional semiconductors by surface-engineered MXenes. J Am Chem Soc 138(49):15853–15856

[25] Liu Y, Stradins P, Wei S-H (2016) Van der Waals metal-semiconductor junction: weak Fermi level pinning enables effective tuning of Schottky barrier. Sci Adv 2(4):e1600069

[26] Liu Y, Wu H, Cheng H-C, Yang S, Zhu E, He Q, Ding M, Li D, Guo J, Weiss NO, Huang Y, Duan X (2015) Toward barrier free contact to molybdenum disulfide using graphene electrodes. Nano Lett 15(5):3030–3034

[27] Zhang J, Xie W, Agiorgousis ML, Choe DH, Meunier V, Xu X, Zhao J, Zhang S (2018) Quantum oscillation in carrier transport in two-dimensional junctions. Nanoscale 10(17):7912–7917

[28] Zhang J, Xie W, Zhao J, Zhang S (2016) Band alignment of two-dimensional lateral heterostructures. 2D Mater 4(1):015038

[29] Popov I, Seifert G, Tománek D (2012) Designing electrical contacts to MoS_2 monolayers: a computational study. Phys Rev Lett 108(15):156802

[30] Kresse G, Furthmüller J (1996) Efficient iterative schemes for ab initio total-energy calculations using a plane-wave basis set. Phys Rev B 54(16):11169–11186

[31] Kresse G, Furthmüller J (1996) Efficiency of ab initio total energy calculations for metals and semiconductors using a plane-wave basis set. Comput Mater Sci 6(1):15–50

[32] Kresse G, Hafner J (1993) Ab Initio molecular dynamics for liquid metals. Phys Rev B 47(1):558–561

[33] Kresse G, Joubert D (1999) From ultrasoft pseudopotentials to the projector augmented-wave method. Phys Rev B 59(3):1758–1775

[34] Klimeš J, Bowler DR, Michaelides A (2009) Chemical accuracy for the van der Waals density functional. J Phys Condens Mat 22(2):022201

[35] Monkhorst HJ, Pack JD (1976) Special points for Brillouin-zone integrations. Phys Rev B 13(12):5188–5192

[36] Taylor J, Guo H, Wang J (2001) Ab Initio modeling of quantum transport properties of molecular electronic devices. Phys Rev B 63(24):245407

[37] Brandbyge M, Mozos J-L, Ordejón P, Taylor J, Stokbro K (2002) Density-functional method for nonequilibrium electron transport. Phys Rev B 65(16):165401

[38] Atomistix ToolKit, version 2019. QuantumWise a/s: Copenhagen, Denmark

[39] Çakır D, Peeters FM (2014) Dependence of the electronic and transport properties of Metal–$MoSe_2$ interfaces on contact structures. Phys Rev B 89(24):245403

[40] Hu Z, Metiu H (2011) Choice of U for DFT + U calculations for titanium oxides. J Phys Chem C 115(13):5841–5845

[41] Perdew JP, Burke K, Ernzerhof M (1996) Generalized gradient approximation made simple. Phys Rev Lett 77(18):3865–3868

[42] Gao S, Yang L (2017) Renormalization of the quasiparticle band gap in doped two-dimensional materials from many-body calculations. Phys Rev B 96(15):155410

[43] Liang Y, Yang L (2015) Carrier plasmon induced nonlinear band gap renormalization in two-dimensional semiconductors. Phys Rev Lett 114(6):063001

[44] Pan Y, Wang Y, Ye M, Quhe R, Zhong H, Song Z, Peng X, Yu D, Yang J, Shi J, Lu J (2016) Monolayer phosphorene-metal contacts. Chem Mater 28(7):2100–2109

[45] Pan Y, Dan Y, Wang Y, Ye M, Zhang H, Quhe R, Zhang X, Li J, Guo W, Yang L, Lu J (2017) Schottky barriers in bilayer phosphorene transistors. ACS Appl Mater Interface 9(14):12694–12705

[46] Zhang X, Pan Y, Ye M, Quhe R, Wang Y, Guo Y, Zhang H, Dan Y, Song Z, Li J, Yang J, Guo W, Lu J (2018) Three-layer phosphorene-metal interfaces. Nano Res 11(2):707–721

[47] Das S, Zhang W, Demarteau M, Hoffmann A, Dubey M, Roelofs A (2014) Tunable transport gap in phosphorene. Nano Lett 14(10):5733–5739

[48] Pan Y, Li S, Ye M, Quhe R, Song Z, Wang Y, Zheng J, Pan F, Guo W, Yang J, Lu J (2016) Interfacial properties of monolayer MoSe2–Metal contacts. J Phys Chem C 120(24):13063–13070

[49] Zhong H, Quhe R, Wang Y, Ni Z, Ye M, Song Z, Pan Y, Yang J, Yang L, Lei M, Shi J, Lu J (2016) Interfacial properties of monolayer and bilayer MoS_2 contacts with metals: beyond the energy band calculations. Sci Rep 6:21786

[50] Huang H, Xing G, Fan X, Singh D (2019) Layered Tl_2O: a model thermoelectric material. J Mater Chem C 7:5094–5103

[51] Liu H, Hu K, Yan D, Chen R, Zou Y, Liu H, Wang S (2018) Recent advances on black phosphorus for energy storage, catalysis, and sensor applications. Adv Mater 30(32):1800295

[52] Yang S, Zhang K, Ricciardulli AG, Zhang P, Liao Z, Lohe MR, Zschech E, Blom PWM, Pisula W, Müllen K, Feng X (2018) A delamination strategy for thinly layered defect-free high-mobility black phosphorus flakes. Angew Chem Int Ed 57(17):4677–4681

[53] Pan Y, Gu J, Tang H, Zhang X, Li J, Shi B, Yang J, Zhang H, Yan J, Liu S, Hu H, Wu M, Lu J (2019) Reexamination of the Schottky barrier heights in monolayer MoS_2 field-effect transistors. ACS Appl Nano Mater 2(8):4717–4726

[54] Liu Y, Guo J, Zhu E, Liao L, Lee SJ, Ding M, Shakir I, Gambin V, Huang Y, Duan X (2018) Approaching the Schottky-Mott limit in van der Waals metal–semiconductor junctions. Nature 557(7707):696–700

[55] Peng Q, Si C, Zhou J, Sun Z (2019) Modulating the Schottky barriers in MoS_2/MXenes heterostructures via surface functionalization and electric field. Appl Surf Sci 480:199–204

[56] Li Y, Lin S, Liu Y, Chai Y, Lau SP (2019) Tunable Schottky barriers in ultrathin black phosphorus field effect transistors via polymer capping. 2D Mater 6(2):024001

Publisher's Note Springer Nature remains neutral with regard to jurisdictional claims in published maps and institutional affiliations.